# NUMERICAL SIMULATION OF SHOCK-WAVE/ BOUNDARY/LAYER INTERACTIONS IN A HYPERSONIC COMPRESSION CORNER FLOW

*A. Pishevar*

*Department of Mechanical Engineering*
*Isfahan University of Technology*
*Isfahan. Iran*

**Abstract** Numerical results are presented for the shock-boundary layer interactions in a hypersonic flow over a sharp leading edge compression corner. In this study, a second- order Godunov type scheme based on solving a Generalised Riemann Problem (GRP) at each cell interface is used to solve thin shear layer approximation of laminar Navier-Stokes (N-S) equations. The calculated flow-field shows general agreement with the experimental data. The heat transfer coefficient and the extent of the separation are predicted with an adequate accuracy. Furthermore, the effects of the employed slope-limiter on the present computations are addressed.

**Key Words** TVD Scheme, Slope-Limiter, Generalised Riemann Problem, Compression Corner Flow

**چکیده** نتایج عددی برای مسئله اندرکنش موج ضربه ای-لایه مرزی در جریان ابر صوتی از روی یک گوشه تراکمی با لبه حمله تیز ارائه می شود. در این بررسی، برای حل معادلات تقریبی لایه نازک ناویر-استوکس از یک روش مرتبه دوم نوع Godunov بر پایه حل مسئله تعمیم یافته ریمان در هر سطح سلولی استفاده می شود. میدان جریان محاسبه شده در این تحقیق تطابق عمومی خوبی را با نتایج آزمایشگاهی نشان می دهد. ضریب انتقال حرارت و دامنه ناحیه جدا شده با دقت مناسب بوسیله نتایج حاضر پیش بینی می گردند. همچنین، اثر تابع محدودکننده شیب بر روی محاسبات ارائه شده مورد توجه قرار می گیرد.

## INTRODUCTION

The compression corner flow can be considered as a simplified model for the flow over control surfaces and the engine inlets of high speed air-breathing vehicles. The shock/boundary layer interactions that occur in the flow field can drastically reduce the effectiveness of these devices or even damage the structure. Therefore, the successful prediction in calculating the aero-thermal loads and the extent of separation for this complex flow is a critical issue in design process. Figure 1 shows schematically the prominent features usually observed in the resultant flow-field. Two kinds of interactions can be identified in this figure. First, a shock is formed at the leading edge due to the displacement of streamlines in the layer near the leading edge where the boundary layer grows smoothly. Second, the corner shock interacts strongly with the bounday layer in a very complex fashion. The high pressure behind the compression waves is felt upstream through the subsonic portion

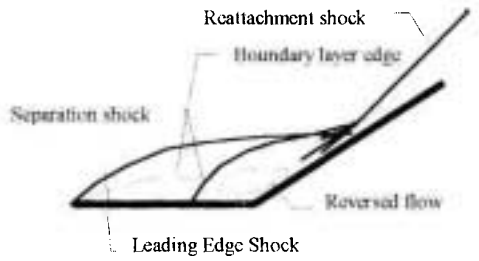


**Figure 1.** Schematic of resultant flow field.

of the layer and causes the flow to separate some distance upstream of the corner. As a result, a shock develops at the separation point and the corner shock moves downstream where the boundary layer reattaches the surface. Furthermore, the corner shock intersects the leading edge shock, resulting in an expansion fan and a slip stream. Downstream of the reattachment point, skin friction and heat transfer rate increase due to the rapid decrease of the boundary layer thickness.

The compression corner flow has been investigated experimentally by several scholars. Holden and Moselle [1] measured the surface quantities and the length of the separated region under a wide range of low-enthalpy conditions. Mallinson et al. [2] studied the possible influences of chemical reactions and other real gas effects for high enthalpy flow. They concluded that under their experimental conditions these effects appear to be negligible and, therefore, theoretical and computational efforts based upon a perfect gas model may lead to accurate results. In addition to its practical advantages, compression corner flow has also become a standard test problem for the validation of many codes, due to the existence of highly accurate benchmark experimental data. Rudy et al. [3] examined the highly separated flow with four different codes and showed that for accurate comparison with experimental data, computational methods need to incorporate three dimensional effects. Taking this point into account, Gaitonde and Shang [4] investigated the accuracy of flux-split algorithms in predicting heat transfer coefficient. They concluded that their computational results could be notably influenced by the choice of slope limiter employed in their calculations.

In the presence of strong discontinuities such as shock waves, numerical treatment of convective fluxes in N-S equations is the most difficult task to cope. Over the last four decades different classes of schemes have been proposed to solve this problem (see for example [5]). The more recent approaches employ the concept of non-linear TVD stability criteria and are second-order accurate in space and time. These schemes are usually called high resolution schemes.

There are different approaches for constructing a high resolution scheme [6-8]. However, a common property can be observed among all TVD schemes: the TVD sufficient conditions are imposed by some kind of limiting procedures called limiters which impose constraints either on the gradient of the dependent variables or on the flux functions.

In this paper, the slope limiter approach is used to construct a second-order numerical algorithm. Generally, the proposed scheme consists of a procedure through which a higher order spatial accuracy is obtained (the linear reconstruction of initial data via a slop limiter function) and a Generalised Riemann Problem (GRP) at each cell interface [9] is solved to obtain the second-order accuracy in time as well.

Although this method is constructed for the one dimensional inviscid equation, its extension to the multi-dimensional viscous problems is accomplished by a fractional-step approach as described in Reference 10.

In the present work, we have also tried to duplicate the flow parameters of the experiment of Holden and Moselle [1]. As a result, the behaviour of different numerical approaches can be assessed consistently by making a comparison between numerical and experimental results. The main objective of the present effort is to examine the accuracy and reliability of the proposed numerical algorithm in complex flow-field. The other objective is to validate the present code by comparing it with experimental and other numerical data.

## 1- BASIC EQUATIONS AND NUMERICAL APPROACH

The two dimensional thin shear layer approximation

of N-S equations in a strong conservative non-dimensional form can be written as:

$$\frac{\partial U^*}{\partial t^*} + \frac{\partial F^{*I}}{\partial x^*} + \frac{\partial G^{*I}}{\partial y^*} + \frac{\partial G^{*v}}{\partial y^*} = 0 \qquad (1)$$

where U* is the vector of conserved variables:

$$U^* = \{ \rho^*, \rho^* u^*, \rho^* v^*, \rho^* e^* \}^t, \qquad (2)$$

$\rho^*$ denotes the non-dimensional density ($\rho/\rho_\infty$), $u^*$ and $v^*$ the non-dimensional Cartesian velocity components ($u/V_\infty$, $v/V_\infty$), and $e^*$ is the non-dimensional total energy defined as $e^* = i^* + 0.5\,(u^{*2} + v^{*2})$, where $i^*$ is the non-dimensional internal energy ($C_v T/V^2_\infty$ for a perfect gas). The non-dimensional coordinates and time are defined as: $x^* = x/L, y^* = y/L, t^* = t/(L/V\infty)$. $F^{*I}$ and $G^{*I}$ are convective fluxes in $x^*$ and $y^*$ directions, respectively, and $G^{*v}$ stands for viscous flux normal to the flow direction:

$$\begin{aligned} F^{*I} &= \{\rho^* u^*, \rho^* u^{*2} + p^*, \rho^* u^* v^*, u^*(\rho^* e^* + p^*)\}^t, \\ G^{*I} &= \{\rho^* v^*, \rho^* u^* v^*, \rho^* v^{*2} + p^*, v^*(\rho^* e^* + p^*)\}^t, \\ G^{*v} &= -\{0, \tau^*_{xy}, \tau^*_{yy}, \tau^*_{xy} u^* + \tau^*_{yy} v^* - \dot{Q}_y\}^t \end{aligned} \qquad (3)$$

The shear stresses and heat fluxes become,

$$\tau^*_{xy} = \frac{\mu^* \partial u^*}{\mathrm{Re}\,\partial y^*}, \quad \tau^*_{yy} = \frac{4\mu^* \partial v^*}{3\mathrm{Re}\,\partial y^*}, \quad \dot{Q}_y = \frac{\mu^*}{(\gamma - 1) M^2_\infty \mathrm{Re}\,\mathrm{Pr}} \frac{\partial T^*}{\partial y^*} \qquad (4)$$

It should be noted that only $y$ derivatives of viscous terms are present in $G^*v$. For air, the Prandtl number Pr is assumed to be 0.72, $\gamma = 1.4$, and the molecular viscosity given by the Sutherland equation as

$$\frac{\mu}{\mu_{ref}} = \left(\frac{T}{T_{ref}}\right)^{3/2} \frac{T_{ref} + S}{T + S} \qquad (5)$$

in which $T$ is the absolute temperature, $\mu_{ref}$, $T_{ref}$ and $S$ are model constants ($\mu_{ref} = 1.789 \times 10^{-5}\ Kg/ms$, $T_{ref} = 288°\ K$, $S = 110°\ K$ ). The eqaution of state for a perfect gas is given by

$$p^* = (\gamma - 1)\left\{\rho^* e^* - \frac{\rho^*}{2}(u^{*2} + v^{*2})\right\}$$

$$T^* = \frac{\gamma M^2_\infty p^*}{\rho^*} \qquad (6)$$

where $p^*$ and $T^*$ are the non-dimensional pressure and temperature, ($p^* = p/\rho_\infty V^2_\infty$, $T^* = T/T_\infty$). The above set of equations is completed by the addition of proper set of initial and boundary conditions.

### 1.1 Numerical Scheme

To develop an efficient numerical algorithm, Equation1 is split at the differential and discrete level in terms of the spatial directions and the physical processes [11]. The proposed method is to time split the equation into a hyperbolic (convection) part and a parabolic (diffusion) part. The hyperbolic part is solved by an explicit second-order Godonov type scheme via the locally one-dimensional time-splitting method of Strang [10]. The parabolic part is solved by an ADI method with central difference in space. Note that for TSL equations, there is only one viscous term. Therefore, discretization of the parabolic part will lead to three diagonal systems of equations which can be converted by a low cost method.

Now, consider the hyperbolic part of Equation 1. It only evolves the solution in time by the convective flux in the $x$ direction (all superscripts are removed from the notation for the sake of simplicity):

$$\frac{\partial U}{\partial t} + \frac{\partial F}{\partial x} = 0 \qquad (7)$$

Integrating Equation 7 over a cell confined to the $[x_{j-1/2}, x_{j+1/2}]$ and the time interval $[t^n, t^{n+1}]$, yields:

$$\overline{U}_j^{n+1} = \overline{U}_j^n - \frac{\Delta t}{\Delta x}\left[\widehat{F}_{j+1/2} - \widehat{F}_{j-1/2}\right] \qquad (8)$$

where $\overline{U}_j^n$ denotes the cell average values at time $t^n$ and $\widehat{F}_{j+1/2}$ is the numerical flux function defined as:

$$\widehat{F}_{j+1/2} = \int_{t^n}^{t^{n+1}} F\left(U\left(x_{j+1/2}, t\right)\right) dt \qquad (9)$$

In the present method, the above fluxes are calculated by a second-order Godunov type scheme as described in Reference 9. Basically, this method is broken into three steps:

• Use the cell average $\overline{U}_j^n$ to define a piecewise linear approximation of the initial condition at time $t^n$:

$$U^n(x, t^n) = \overline{U}_j^n + \frac{x - x_j}{2} S_j^n \quad \text{for} \quad x \in [x_{j-1/2}, x_{j+1/2}] \qquad (10)$$

• Solve the conservation laws Equation 7 exactly with the above initial conditions in each cell for a sufficiently small time interval $t^n < t < t^{n+1}$

• Compute all averages of the resulting solution at $t^{n+1}$ to obtain $\overline{U}_j^{n+1}$ by Equation 8.

A necessary condition for this algorithm, which is of second-order accuracy, is that the slopes $S_j^n$ are locally weighted averages of forward and backward differences. On the other hand, to avoid spurious oscillations, a constraint should be imposed on the amount of slope in each cell by an appropriate limiter function. In most of the following computations, the Monotonised Central Difference (MCD) slope-limiter, which was given in the context of the MUSCL scheme by van Leer [7], is used:

$$S_j^n(a_j, b_j) = \text{min mod}\left(\frac{a_j + b_j}{2}, 2 \text{ min mod}\left(a_j, b_j\right)\right) \qquad (11)$$

where $a_j$, $b_j$ denote the forward and backward differences

$$a_j = \frac{\overline{U}_{j+1}^n - \overline{U}_j^n}{\Delta x}, \quad b_j = \frac{\overline{U}_j^n - \overline{U}_{j-1}^n}{\Delta x} \qquad (12)$$

and the minmod function is defined by

$$\text{min mod}(a,b) = \begin{cases} a & \text{if} \quad |a| \le |b|, \ ab \ge 0 \\ b & \text{if} \quad |a| \ge |b|, \ ab > 0 \\ 0 & \text{if} \quad ab \le 0 \end{cases} \qquad (13)$$

A more diffusive limiter function is the Min Mod (MM) limiter defined as

$$S_j^n = \text{min mod}\left(a_j, b_j\right) \qquad (14)$$

The piecewise linear form of the initial conditions (Equation 10) may introduce discontinuities at the each cell interface $x_{j+1/2}$. Thus, exact solution to the Equation 7 consists of a sequence of Generalised Riemann Problem [9] at the cell interfaces. For Equation 8 which is of second-order accurate in time, the numerical flux $\widehat{F}_{j+1/2}$ (Equation 9) should be evaluated at mid-time step ($j + 1/2$, $\Delta t/2$) at a cell interface as

$$\widehat{F}_{j+1/2} = F_{j+1/2}^R + \frac{\Delta t}{2}\left(\frac{\partial F}{\partial t}\right)_{j+1/2}^n \qquad (15)$$

Here, $F_{j+1/2}^R$ denotes the flux contribution from a Riemann solver using solely the interface variable values. An approximate Riemann solver based on two simple acoustic waves is used in the smooth part of the flow while the algorithm switches to an exact Riemann solver near the discontinuities. However in the later case, the approximate solution by the two acoustic wave models can still be used as an initial guess in the iterative procedure [12]. The time derivatives in Equation15 depend on the pattern of waves emanating from the discontinuities at initial time $t = 0^+$ and given in a closed form by Ben-Artzi and Falcovitz [9]. The stable time step size $\Delta t$ should be restricted by a CFL like condition as

$$\frac{\Delta t}{\Delta x} |F'(U)|_{\max} \le 1 \qquad (16)$$

where $|F'(U)|_{\max}$ is the magnitude of the globally

largest characteristic speed. This restriction on the time steps ensures that the emanating wave from one interface never crosses the neighbouring interfaces. The same procedure can be used to treat the convective fluxes in the $y$ direction.

As noted earlier, the above algorithm is extended to multi-dimensional viscous problems by a fractional-step approach. Let $L_x^{\Delta t}$, $L_y^{\Delta t}$ be the locally one-dimensional split hyperbolic operator which evolves the solution by the time step $\Delta t$ in the $x$ and $y$ directions. Furthermore, let $L_{yv}$ be the implicit split parabolic operator in the $y$ direction. Then a fractional-step method for the TSL Equation 1 will look like

$$\bar{U}_{jk}^{n+2} = L_{yv}^{\Delta t} L_y^{\Delta t} L_x^{2\Delta t} L_y^{\Delta t} L_{yv}^{\Delta t} \bar{U}_{jk}^{n} \tag{17}$$

where $L_x^{\Delta t} \bar{U}_{jk}^{n}$, for example, is

$$L_x^{\Delta t} \bar{U}_{jk}^{n} = \bar{U}_{jk}^{n} - \frac{\Delta t}{\Delta x} [\hat{F}_{j+1/2,k} - \hat{F}_{j-1/2,k}] \tag{18}$$

with $\hat{F}_{j+1/2,k}$ defined in Equation 15. Now, the stable time step in both directions is given by

$$\Delta t = \frac{\Delta t_x \Delta t_y}{\Delta t_x + \Delta t_y} \tag{19}$$

where $\Delta t_x$, $\Delta t_y$ are the stable time steps in $x$ and $y$ directions, respectively, given by Equation 16. This ensures that the composite time step is smaller than the split one dimensional stable time steps.

The above algorithm can be extended to the case of arbitrary quadrilateral grids. In such a case, the locally one-dimensional split operator, which now solves Riemann problem in the direction of the normal to the cell edges in the physical space, sweeps the grids in the computational coordinates of $j$ and $k$. In such a case, the limiter function is imposed on the directional derivatives in the local curvilinear coordinates.

### 1.2 Computational Domain and Mesh

In the present study, a two dimensional wedge with 24 degree corner angle and a leading edge distance of L=0.44m is considered. Computations were performed on three meshes of $120 \times 40$, $180 \times 60$, $240 \times 80$ grids constructed by an algebraic approach. The coarsest grid was clustered near the corner in the streamwise direction by a stretching factor of $\beta_x = 3.0$ and also in vertical direction near the solid surface by $\beta_y = 1.007$. The second and the third grids with higher resolution were constructed from the first grid using, respectively, 50 and 100 percents additional points in both directions while maintaining the same grid stretching. The coarsest mesh used in the calculation is shown in Figure 2. In this figure, the $x$ axis is normalised by the leading distance as $X = x/L$.

### 1.3 Boundary and Initial Conditions

The boundary conditions are considered as follows; at inflow boundaries, the flow variables are held constant at the free-stream state; at solid boundaries the velocity components and the normal pressure gradient are set to zero; at the outflow boundary, the flow is predominately supersonic and therefore, the zero order extrapolation of flow variable from the inside of the computational domain is sufficient.

To compare with the other experimental evidence and also numerical results [3,4], the free stream parameters are considered as follows; $T_\infty = 72.7\ K$,

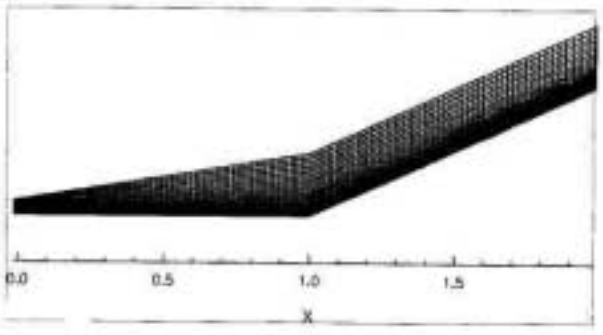


**Figure 2.** Computational grid.

$p_\infty = 10.1\ N/m^2$, free stream Reynolds number per unit length $\mathrm{Re} = 2.4 \times 10^5$, $M_\infty = 14.1$. The solid wall is held at the isothermal condition with $T_w = 297.22K$. The initial condition is assumed to be uniform and equal to the free stream condition.

## 2. RESULT AND DISCUSSION

The computations were performed on a Pentium 166 with 32 MB of memory. With the middle grid, each run takes approximately 20 hours. Calculation is terminated when the computational time reaches to $5\times10^{-3}$s. By this time interval the residual in the density field will be less than $10^{-5}$. Figure 3 displays the calculated pressure contours in the flow-field with the finest grid and the MCD limiter function. In this figure, to amplify all present waves with different strengths, the pressure contours are not equally spaced between the minimum and the maximum values. Generally, a good agreement can be seen between the present computation and the flow-field pattern described earlier. Streamlines are shown in Figure 4. The flow separation point, the reversed flow region, and the boundary layer reattachment point are demonstrated well by this figure. It should be noted that the accurate prediction of separation extent depends on the grid resolution in the normal direction to the solid surface. In this simulation, the first point is placed at $y^+ = y\,\rho_w\,(\tau_w/\rho_w)^{1/2}/\,\mu_w < 2$.

The surface quantities are compared with those of the experiment in Figures 5 to 7. The surface pressure coefficient, defined as $c_p = 2(p_w - p_\infty)/(\rho_\infty V_\infty^2)$, is shown in Figure 5. Here, the abscissa is the dimensionless distance along the surface from the leading edge (X=S/L, L=0.44m). As shown in this figure the solution is almost converged on the second grid. The first rise in the pressure coefficient is calculated accurately and its position (**X**~0.55) is in very good agreement with that of the experiment. However, the maximum pressure coefficient is about 16% over-estimated. Figure 6 displays a comparison between the calculated skin friction coefficient, defined as $2\tau_w/2(\rho_\infty u_\infty^2)$, and that of the experiment. Negative skin friction values determine the size of the separated reverse flow region. As can be seen the extent of separated region is predicted with adequate accuracy but the maximum and minimum skin friction values are not in complete agreement with the experiment. Finally, the heat transfer coefficient, defined as $k(\partial T/\partial n)_w/\{\rho_\infty u_\infty (h_0 - h_\infty)\}$ where $h$ is the total enthalpy, is shown in Figure 7. Here again the peak heat transfer coefficient is calculated higher than its experimental value. However, general agreement still exits between the computation and the experiment. The deviation of all surface coefficients from their experimental values may have an origin of three dimensional effects as discussed by Rudy et al. [3].

Numerical experiments of this flow-field by other

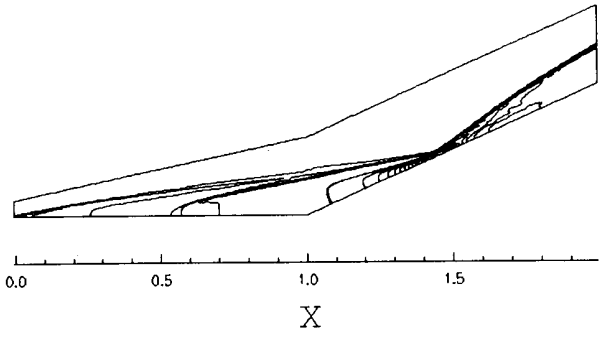


**Figure 3.** Pressure contours.

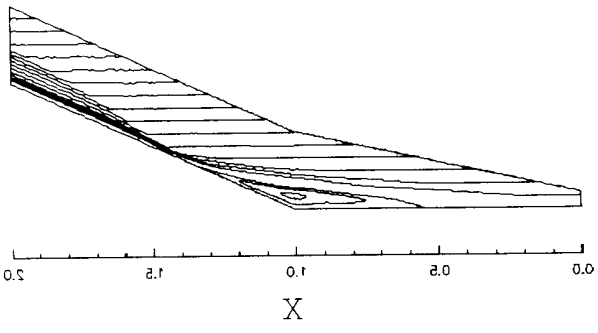


**Figure 4.** Stream lines.

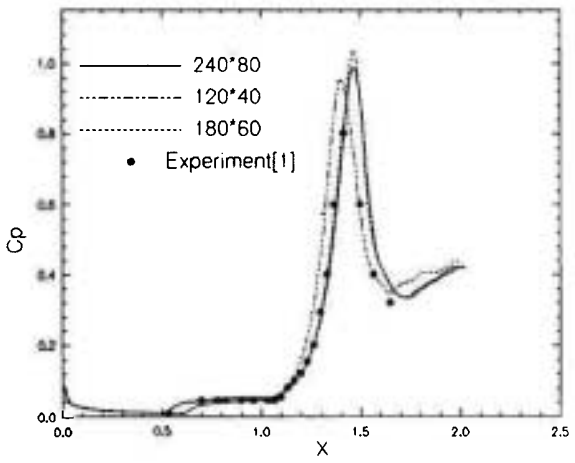


**Figure 5.** Surface pressure coefficient, experiment from Holden et al. [1].

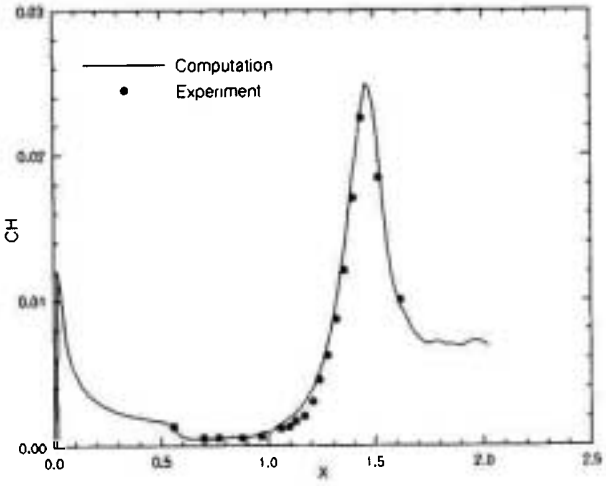


**Figure 7.** Heat transfer coefficient, experiment from Holden et al. [1].

researchers revealed that the solution may be highly influenced by the choice of the slope limiter. Gaitonde et al. [4] investigated the behaviour of three limiters using the Roe's scheme with a third order procedure and the thin shear layer approximation for the viscous terms. They pointed out that the separation extent and peak surface quantities are clearly sensitive to the type of limiter. The most accurate results in their calculations were obtained by the less compressive minmod limiter. This conclusion exhibits contrast to the other numerical experiment with the advection model equation [13] or the Euler equations [14]. They also reported that by refining the grid, a larger separated region than that observed experimentally was predicted. The effects of slope-limiter on the present numerical results are shown in Figures 8,9 and Table 1. Here, only the MCD and MM limiters (the first is typically a compressive limiter and the

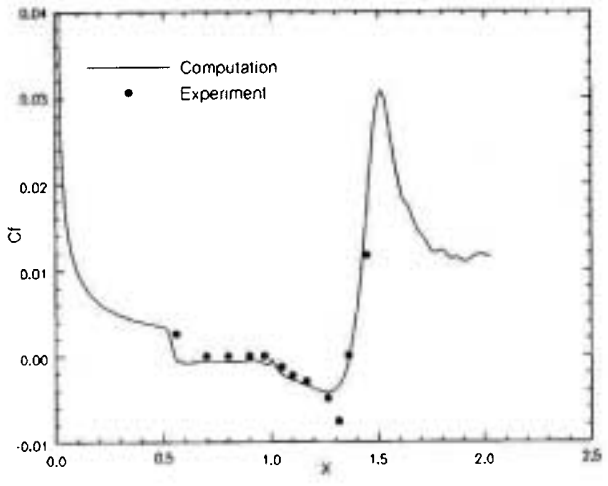


**Figure 6.** Skin friction coefficient, experiment from Holden et al. [1].

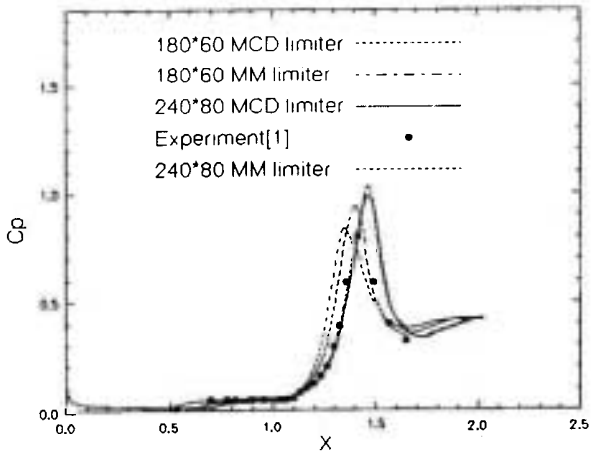


**Figure 8.** Effects of limiter function and grid resolution on the pressure coefficient.

| | |
|---|---|
| $Q$ | heat transfer rate |
| Re | Reynolds Number |
| $S_j^n$ | slope limiter function |
| T | temperature |
| $u, v$ | Cartesian velocity components |
| $U$ | vector of conserved variables |
| $\overline{U}_j^n$ | cell average of conserved variables |
| S | model constant in Sutherland viscosity equation |

## Greek Symbols

| | |
|---|---|
| $\beta$ | grid stretching factor |
| $\gamma$ | specific heat ratio |
| $\mu$ | molecular viscosity |
| $\rho$ | density |
| $\tau$ | shear stress |
| $\Delta$ | increment in time or space |

## Subscripts

| | |
|---|---|
| $j, k$ | cordinates in discretized computational domain |
| *ref* | reference state |
| $\infty$ | free stream state |

## Superscripts

| | |
|---|---|
| n | time level |
| R | Solution to Riemann problem |
| * | non-dimensional parameters |

## Abbreviations

| | |
|---|---|
| **ADI** | Alternative Direction Implicit |
| **CFD** | Computational Fluid Dynamics |
| **CFL** | Courant-Friedrichs-Lewy condition |
| **GRP** | Generalised Riemann Problem |
| **MCD** | Monotonised Center Difference limiter |
| **MM** | MinMod limiter |
| **MUSCL** | Monotone Upstream Scheme for Conservation Laws |
| **N-S** | Navier-Stokes equations |
| **TSL** | Thin Shear Layer approximation of N-S equations |
| **TVD** | Total Variation Diminishing |

## REFERENCES


1. M. S. Holden, and J. R., Moselle, "Theoretical and Experimental Studies of the Shock Boundary Layer Interaction on Compression Surfaces in Hypersonic Flow", Rept. ARL 70-0002, Wright-Patterson AFB, OH, (Jan. 1970).
2. S. G. Mallinson, S. L. Gai and N. R. Mudford, "High-Enthalpy, Hypersonic Compression Corner Flow," *J. AIAA*, 34, (1996).
3. D. H. Rudy, J. L. Thomas, A. Kumar and A. Gnoffo, "Computation of Laminar Hypersonic Compression-Corner Flows," *J. AIAA*, 29, (1991).
4. D. Gaitonde and J. S. Shang, Accuracy of Flux-Split Algorithms in High-Speed Viscous Flows," *J. AIAA*, 31, (1993).
5. P. Woodward and P. Colella, Review Article, "The Numerical Solutions of Two-dimensional Fluid Flow with Strong Shocks," *J. Comp. Phys.* 54, (1984).
6. J. P. Boris and D. L. Book, "Flux Corrected Transport, A Fluid Transport Algorithm that Works," *J. Comp.Phys.*, 55, (1984).
7. B. van Leer, "Toward the Ultimate Conservative Difference Scheme v, A Second-Order Sequel to Godonuv's Method," *J. Comp.* 32, (1979).
8. A. Harten, "High Resolution Schemes for Hyperbolic Conservation Laws," *J. Comp. Phys.*, 49, (1983).
9. M. Ben-Artzi and J. Falcowitz, "A Second-Order Godonuv-Type Scheme for Compressible Fluid Dynamics," *J. Comp. Phys.*, 55, (1984).
10. H. C. Yee, R. F. Warming and A. Harten, "Implicit Total Variation Diminishing (TVD) Schemes for Steady State Calculation, "*J. Comp. Phys.*, 57, (1985).
11. N. N. Yanenko and V. M. Kovenya, "The Splitting Method for the Numerical Solution of Gas Dynamics, Numerical Methods in Fluid Dynamics, "MIR Publisher, (1984).
12. J. J. Gottelieb and C. P. T. Groth, "Assessment of Riemann Solvers for Unsteady one Dimensional

Inviscid Flows of Perfect Gases," *J. Comp. Phys.*, 78, (1988).

13. C. D. Munz, On the Numerical Dissipation of High Resolution Schemes for Hyperbolic Conservation Laws," *J. Comp. Phys.*, 77, (1988).
14. A. R. Pishevar, "Higher Order Computation of Unsteady State Compressible Flow, "PhD Thesis, Imperial College of Science and Technology, (1995).